

Contents lists available at ScienceDirect

Advanced Powder Technology

journal homepage: www.elsevier.com/locate/apt



Original Research Paper

Structural and mechanical characterization of lithium-ion battery electrodes via DEM simulations



Clara Sangrós Giménez a,b,*, Benedikt Finke , Christine Nowak b, Carsten Schilde , Arno Kwade b, Christine Nowak b, Carsten Schilde , Arno Kwade b, Christine Nowak b, Carsten Schilde b, Arno Kwade b, Christine Nowak b, Carsten Schilde b, Christine Nowak b, Carsten Schilde b, Arno Kwade b, Christine Nowak b, Carsten Schilde b, Christine Nowak b, Christin

^a Institute of Particle Technology, Technische Universität Braunschweig, Volkmaroder Straße 5, 38104 Braunschweig, Germany

ARTICLE INFO

Article history: Received 20 September 2017 Received in revised form 3 May 2018 Accepted 10 May 2018 Available online 19 May 2018

Keywords:
Discrete element method
Lithium-ion battery electrodes
Microstructure
Mechanical characterization
Simulations

ABSTRACT

Electrode structural stability and mechanical integrity is of major importance regarding not only lithiumion battery performance but also safety aspects. The goal of this study is to design a simulation procedure to reproduce the microstructural and mechanical properties of such lithium-ion battery electrodes. Taking into consideration the particulate state of these electrodes, a discrete element method (DEM) approach is proposed, which comprises a procedure to reproduce real electrode structures and the application of a proper contact model to capture the bulk mechanics. This is accomplished by considering particle interactions as well as the performance of the binder. Three different electrodes are manufactured with the aim of calibrating and validating the Hertzian-bond contact model. Experimental nanoindentation measurements prove to be in good agreement with the simulation outcome, concluding that the method constitutes a valuable physical and mechanical basis for further applications.

© 2018 The Society of Powder Technology Japan. Published by Elsevier B.V. and The Society of Powder Technology Japan. All rights reserved.

1. Introduction

Lithium-ion batteries (LIBs) are widely used as electrochemical power sources for mobile telephones, personal computers, cameras and other modern-life appliances. They are also remarkably successful in the electric power vehicle market due to their long life cycles and high-rate capabilities. However, as lithium-ion batteries increase in popularity, there is still room to improve their performance and durability. Within this framework, the importance of electrode structural stability and mechanical integrity has been already pointed out by several research groups. Peterson et al. [1] experimentally investigated the effect of several relevant structural factors on electronic and ionic conductivity. By presenting various scenarios, it was demonstrated that electronic conductivity is greatly increased by raising the carbon black volume fraction and reducing the electrode porosity, whereas the ionic conductivity decreases by increasing the amount of carbon black and binder. Among other interesting results, Bockholt et al. [2] showed that the positive or negative impact of calendering on battery performance is directly linked to the change in the structure of the electrode. With regard to active material particle size, Michaels et al. [3] experimentally confirmed that smaller particles give rise to higher electrode adhesive strength and lower electrode conductivity.

Concerning mechanical aspects of lithium-ion battery electrodes, it is well-known that stress generation within the electrodes is one of the main causes for capacity fade and eventual failure of lithium-ion batteries. For this reason, mechanical instabilities, including structure disintegration and particle fracturing, loss of contact between the electrode and the current collector or plastic deformation have been a major subject of extensive research activities [4–6]. In this regard, the work of Mukhopadhyay et al. [7] must be noteworthy underlined. They presented an overview of the sources and relative magnitudes of stresses within the electrodes and introduced recently developed techniques for *in situ* measurements of stress evolution.

Since experimental research implies costly processes in terms of raw materials, resources and time, modelling and numerically simulating lithium-ion batteries have been recently in the spotlight as an alternative approach [9–11]. Bearing in mind the effect of electrode microstructure on voxel performance, numerical methods have specifically become more popular due to the additional complexity of experiments. In order to be able to model the electrode microstructure accurately, it is necessary to acknowledge the particulate nature of such structures. So far, this fact has been only partially contemplated. Within this context, this work proposes a discrete element method (DEM) approach. This method,

^b Battery LabFactory Braunschweig, Technische Universität Braunschweig, Langer Kamp 8, 38106 Braunschweig, Germany

^{*} Corresponding author at: Institute for Particle Technology, Technische Universität Braunschweig, Volkmaroder Straße 5, 38104 Braunschweig, Germany.

E-mail address: c.sangros@tu-braunschweig.de (C. Sangrós Giménez).

first developed by Cundall and Strack [8], is based on the characterization of contacts between a number of discrete particles forming the bulk material. Even though its application to electrode simulations is to date in an early phase, DEM has been already proven to be a feasible tool in the subject. Schneider et al. [9] analyzed the effect of electrode thickness and composition on the Triple Phase Boundary (TPB) length by computing several composite electrodes consisting of spherical monosized particles. Liu et al. [10] generated various numerical microstructures by sintering in order to assess the importance of macroscopic porosity and pore surface area of SOFC (Solid Oxide Fuel Cells) electrodes. Also in this line of research, Forouzan et al. [11] developed a mesoscale particlebased simulation technique to predict the microstructure of lithium-ion battery electrodes considering the manufacturing process. These contributions have helped to improve the understanding of fundamental structural parameters such as electrode porosity, thickness or composition on the voxel performance. Nevertheless, they constitute an overall approximation of the real microstructure. In particular, the mechanical characteristics, which are directly affected by the structure, have not been fully comprehended for lithium-ion battery electrodes so far.

In the scope of this work, the focus is set on designing a simulation procedure and an appropriate DEM contact model that can reproduce not only the microstructure but also the mechanics of lithium-ion battery electrodes. Combining simulations with nanoindentation experiments, the contact model is calibrated and validated, bringing reliability to the developed method. It is believed that this study offers an interesting tool which constitutes an accurate structural and mechanical foundation for future investigations. For instance, with the aim of studying stress evolution within electrodes during lithium-ion intercalation or investigating the effect of manufacturing processes such as calendering.

This work is organized as follows: In Section 2, the DEM contact model is fully explained. Section 3 includes the numerical generation of the electrode microstructures. For calibration and validation, several electrodes were manufactured; Section 4 briefly introduces the materials as well as the experimental characterization. Simulation results are gathered in Section 5. Concluding, the outcomes are summarized.

2. Materials and experimental characterization

In the scope of this contribution, three electrodes were manufactured and physically characterized; one electrode for calibrating the contact model (C1), and the other two for validating the simulation results (V1 & V2).

The composite anode electrodes were prepared with MesoCarbon MicroBeads graphite powder (MCMB, Osaka) as active material and a mixture of styrene-butadiene copolymer (SBR, Lipaton SB 5521, Synthomer) and carboxymethyl voxelulose (CMC, Walocel Na-CMC2000 PA, Dow Wolff Voxelulosics GmbH) as binder. The

MCMB powder and the CMC were firstly dry-mixed for 15 min in a rotary drum mixer (Turbula® T2F, Willy A. Bachofen Corp.) with a rotational speed of 49 min⁻¹ for 15 min. The mixture was then dispersed in deionized water for 70 min using a dissolver (Dispermat CA, VMA Getzmann) with a 50 mm toothed disk. The circumferential velocity of the disk was set to 9 m s⁻¹ and vacuum was applied during additional 10 min right after adding the necessary amount of SBR. The resulting suspensions were coated on a 10 μm copper foil using a continuous pilot-plant scale coater (Labco, Krönert GmbH & Co KG) with a comma bar reverse roll application system. Drying was performed in a three stage convective drying process (Drytec, Hamburg, Germany) at a temperature of 65 °C. The coating and drying speed was set to 2 m min⁻¹. The active material mass loading for all anodes was set to 8.7 ± 1.2 mg cm⁻².

With the aim of assuring reliable simulation results, active material was analyzed via laser diffraction to acquire the particle size distribution. Moreover, porosity of the electrodes was determined by means of mercury intrusion and electrode thickness was measured via a digital gauge, as explained in [12]. Table 1 gathers these outcomes as well as additional information regarding electrode composition. Taking anode C1 as the reference, anode V1 was composed of coarser particles maintaining the same composition. Anode V2 was manufactured with the same active material particle size but with a higher amount of binder. Due to these variations, all three electrodes showed different values of porosity and thickness.

The micromechanical properties were characterized via nanoindentation (UNAT, Asmec Advanced Surface Mechanics GmbH) using a flat punch indenter with a diameter of 100 μm . The compressions (80 measuring points per electrode sample) were performed by controlling the maximum indentation displacement under a constant velocity of 0.15 $\mu m \, s^{-1}$ during both loading and unloading. As suggested by Fischer-Cripps et al. [13], a total displacement of 10% of the coating thickness was chosen in order to avoid substrate effects. The plastic (Wpl), elastic (Wel) and total (Wtot) deformation energies can be calculated based on the force-displacement curves as follows:

$$W_{tot} = \int_0^{h_{max}} F_{load}(h)dh \tag{1}$$

$$W_{el} = \int_{h_f}^{h_{max}} F_{unload}(h) dh \tag{2}$$

$$W_{pl} = W_{tot} - W_{pl} \tag{3}$$

where h_{max} is the maximum displacement during indentation, h_f is the residual indentation depth and F_{load} and F_{unload} are the indentation forces during loading and unloading respectively. Fig. 1 shows exemplarily an experimental force-displacement curve of a nanoindentation measurement.

Table 1Structural parameters of the manufactured electrodes: Anode composition, thickness, porosity as well as active material particle size.

Parameter	Anode used for the calibration (C1)	Anode used for the validation (V1)	Anode used for the validation (V2)
Anode composition (AM/Binder, wt.%)	96:04	96:04	92:08
Anode thickness, he	76.50 μm	79.86 μm	96.43 μm
Porosity, ε	0.45	0.59	0.59
Active material particle size	$x_{10,3} = 4.03 \mu m$	$x_{10,3} = 10.34 \mu\text{m}$	$x_{10,3} = 4.03 \mu m$
	$x_{50,3} = 5.99 \mu m$	$x_{50,3} = 17.45 \mu m$	$x_{50,3} = 5.99 \mu m$
	$x_{90,3}$ = 8.94 μ m	$x_{90,3} = 30.89 \mu m$	$x_{90,3} = 8.94 \mu m$

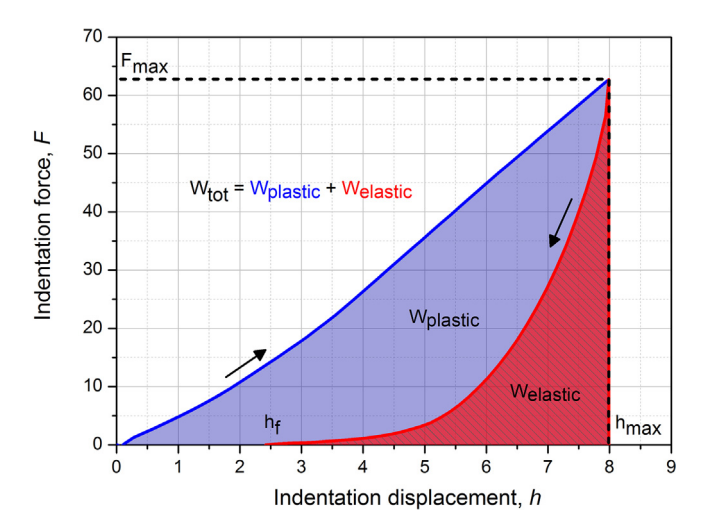


Fig. 1. Force-displacement curve of a nanoindentation measurement.

3. Methodology

3.1. Hertzian-bond contact model

As it was described above, lithium-ion electrodes were composed of mesocarbon microbeads (MCMB) particles embedded in a binder matrix of styrene-butadiene copolymer (SBR) and carboxymethyl voxelulose (CMC) and coated on a current collector made of copper. In this work, a Hertzian-bond contact model is developed to capture the mechanical response of the electrode by combining both MCMB particle and SBR/CMC binder stiffness. This model is based on the Hertz contact model [14] and the bonded particle model proposed by Potyondy and Cundall [15], which is based on a transfer of normal and tangential forces with an additional torque transfer through bonds. Thereby, the elastoplastic behavior of the electrodes can be described based on the force-displacement relationship at single particle level and further implementation of solid bonds under certain conditions.

Hertz [14] developed an elastic force model for the contact between two spheres of isotropic material. However, as it has been examined via single particle nanoindentation, MCMB particles are elasto-plastic in nature, i.e., energy is lost during particle overlay. This energy dissipation due to plastic deformation is modeled using a velocity-dependent damping factor. The contact force in normal and tangential direction is therefore calculated as follows:

$$F = (k_n \delta_n - \gamma_n \upsilon_n) + (k_t \delta_t - \gamma_t \upsilon_t)$$
(4)

where the first term describes the normal force (spring and damping force) and the second term corresponds to the tangential force (shear and damping force) between two interacting particles. k_n and k_t represent the elastic constant for normal and tangential contact accordingly, while γ_n and γ_t describe the viscoelastic damping constant in both directions. v_n and v_t are the normal and tangential component of the relative velocity, δ_n corresponds to the normal overlap and δ_t is the tangential contact displacement, as it is determined in the work of Zabulionis et al. [16]. Since the MCMB particles are embedded in the binder matrix, no friction is regarded in order to reflect the conceivably lubricative state of the particulate network. The elastic stiffness, k_n , is defined as

$$k_n = E^* \sqrt{R^*} \delta_n^{(1/2)} \tag{5}$$

with E^* and R^* being the effective Young's modulus and effective radius, respectively [17]. Resulting from Eqs. (4) and (5), the contact normal force becomes proportional to the particle overlap (δ_n)

raised to the power of 1.5, which makes the model non-linear. Further description of tangential forces, damping forces and respective equations are fully described by Beinert et al. [18].

Aside from active material particles, the binder represents an essential part of the electrode formulation because it maintains the physical microstructure assuring the connectivity of active material particles. Hence, the binder performs a major role in the mechanics of the system and undoubtedly must be contemplated for the simulations. For this study, a mixture of styrene-butadiene copolymer (SBR) and carboxymethyl cellulose (CMC) was used, which shows an elasto-plastic behavior in the operational temperature range of a lithium-ion battery. As it has been reported by Lim et al. [19], a network of active material particles is built, in which the binder matrix spans the whole system connecting the particles via a bridging mechanism. Consequently, it was decided to compute solid bonds between MCMB particles once the structure was defined in order to include the effect of the binder phase.

Bonds were considered cylindrical spring-dashpot elements possessing no mass. A bond is created between two particles, i and j with radii r_i and r_j , if the distance between both of them (L_{ij}) fulfills the following condition:

$$L_{ij} < (r_i + r_j) + (r_i + r_j)f_b \tag{6}$$

where f_b is a factor which controls the number of bonds that are formed during the simulation. Consequently, it is directly related to the real amount of binder used in the experimental formulation of the electrode. The calibration of this parameter is performed with a custom-built numerical tool: once the particle packing is completed and the bonds are created for an initial selected f_b , the distance between two-bonded particles is computed by collecting the position of all individual particles and accounting for the combination of bonded particles. Considering bonds have a cylindrical form, their volume is approximated as $\pi r_{ii}^2 L_{ij}$. The percentage of binder is then reckoned as the sum of all bond volumes divided by the whole electrode volume. An iterative procedure is followed until the binder content in the real electrode structure is achieved. The value of f_b ranges from 0 (no bonds are present) to 1. Likewise, a statistical distribution of bonds within the assembly is assured in order to reduce the likelihood of bond formation without modifying this condition and still balancing the binder content. Bonds are considered to have a virtual radius, r_{ii} , which depends on the radii of the particles and is constant during the simulation:

$$r_{ij} = \frac{r_i \cdot r_j}{r_i + r_i} \tag{7}$$

Thus, the bond radius would be half the particle radius for two bonded particles with same radius. On the one hand, the number of bonds can be controlled. On the other hand, contrary to the original bonded particle novel [15], the radius of each bond does not have to be defined prior to the simulation, as it is automatically set depending on the particles. This constitutes a great advantage specially when dealing with polydisperse systems.

Apart from the already cited contact forces, solid bonds are able to transfer forces between particles as well as an additional torque. The increments of normal bond force dF_n and tangential bond force dF_t are calculated every time step dt, along with the bond torques in normal and tangential direction, dM_n and dM_n :

$$dF_{b,n} = -\nu_n \cdot S_n \cdot A \cdot dt \tag{8}$$

$$dF_{b,t} = -v_t \cdot S_t \cdot A \cdot dt \tag{9}$$

$$dM_{b,n} = -\omega_n \cdot S_n \cdot \frac{J}{2} \cdot dt \tag{10}$$

$$dM_{b,t} = -\omega_t \cdot S_t \cdot J \cdot dt \tag{11}$$

where A is the cross sectional area of the bond, J is the polar moment of inertia, v_n and v_t represent the normal and tangential linear velocities, and ω_n and ω_t correspond to the normal and tangential angular velocities. Both linear and angular velocities are reckoned as relative values given the velocities of the two bonded particles. S_n and S_t are the normal and tangential area-related stiffness of the solid bond, which represent its resistance to deformation. In this enhanced Hertzian-bond contact model, besides the viscoelastic damping term associated to the original Hertz contact model, local non-viscous damping is implemented to represent the energy dissipation of the bond. Thus, the parallel bonds do not behave as a set of springs bringing only an increment of elastic force and moment, but instead they also contribute to the energy loss in the system. The non-viscous damping formulation, implemented to bond forces and torques, is given by:

$$\varphi_b = \alpha \cdot \varphi'_{b_n} + d\varphi_b \tag{12}$$

This expression is independently applied to each degree of freedom. φ_{b_n}' is the magnitude of the unbalanced force or torque, $d\varphi_b$ represents the increment calculated as described in Eqs. (8)–(11), and α is the damping coefficient that needs to be specified. The adjustment of this coefficient is extremely complicated due to the impossibility of acquiring this value experimentally.

Additionally, the ultimate tensile strength that the bond can withstand before breaking must be specified in normal and tangential directions, $\sigma_{max,n}$ and $\sigma_{max,t}$. Thus, the bond breaks and the corresponding forces and torques terminate if one of these two values is exceeded. Under these circumstances, the forces and torques acting on particles in contact will be calculated according to the Hertzian model. Values of normal and tangential tensile strengths, σ_n and σ_t , are determined every time step according to the classical beam theory:

$$\sigma_n = \frac{F_n}{A} + 2 \cdot \frac{M_t}{I} \cdot r_{ij} \tag{13}$$

$$\sigma_t = \frac{F_t}{A} + \frac{M_n}{J} \cdot r_{ij} \tag{14}$$

Bond characteristics as well as bond forces are displayed in Fig. 2a and b. A representative force vs. overlap curve regarding the interaction of two particles subjected to the Hertzian-bond model is shown in Fig. 2c. As it can be seen, before the particles come into contact ($\delta = 0$), there is a repulsive force arising from

the presence of the bond. Thus, the model shifts from a zero to a non-zero force at zero overlap. It must be noted, that there are already some available DEM models which may be in principle valid as well. For instance, Luding contact model, valid for elastoplastic and adhesive contacts, or Edinburgh Contact Model (ECM), which is an elasto-plastic hysteretic contact model [20,21]. However, due to the nature of granular electrode structures, not only the physical contact between particles but also the mechanical behavior of the binder must be considered. Since the deformation and breakage of bonds are the fundamental facts dominating the bulk behavior under these simulation conditions, the enhanced Herztian-bond model is deemed more appropriate.

3.2. Numerical method to generate particulate electrode structures

Previous to generating the electrode structure numerically, it was necessary to experimentally characterize the electrodes, as it was explained previously. Considering the laser diffraction measurements, five representative particle sizes were used for each simulation structure. The total quantity of each was calculated regarding the particle size distribution, the electrode porosity and the electrode thickness.

Electrode microstructures were generated using the open source discrete element method simulation software LIGGGHTS, which is based on the classical molecular dynamics simulator LAMMPS [22]. The procedure to create such structures is depicted in Fig. 3. Firstly, the spherical particles were randomly packed within a rectangular domain. Due to computational limitations, it is currently too costly to simulate a complete electrode on the microscale. For this reason, both boundaries in X and Y direction were held periodic to reduce the size of the simulation domain. The representative volume was fixed in Z direction by introducing a plane under the particles (Z = 0) emulating the current collector. Since it is not feasible to directly create densely packed structures in LIGGGHTS, the initial size of the particles was half the real size. This initial packing was generated with the constraint that particles were not in contact. Afterwards, the radii of the particles were gradually increased until the actual particle size was achieved. This step was critical to originate a valid structure and thus, the growth rate was determined in such manner that the overlap between particles was in no case higher than 10^{-5} % of both particle radii. Accordingly, by setting a proper particle growth rate, high energy increase within the boundaries could be avoided and ultimately, a stable system could be assured while keeping a reasonable CPU time. This novel methodology, as opposed to that employed by

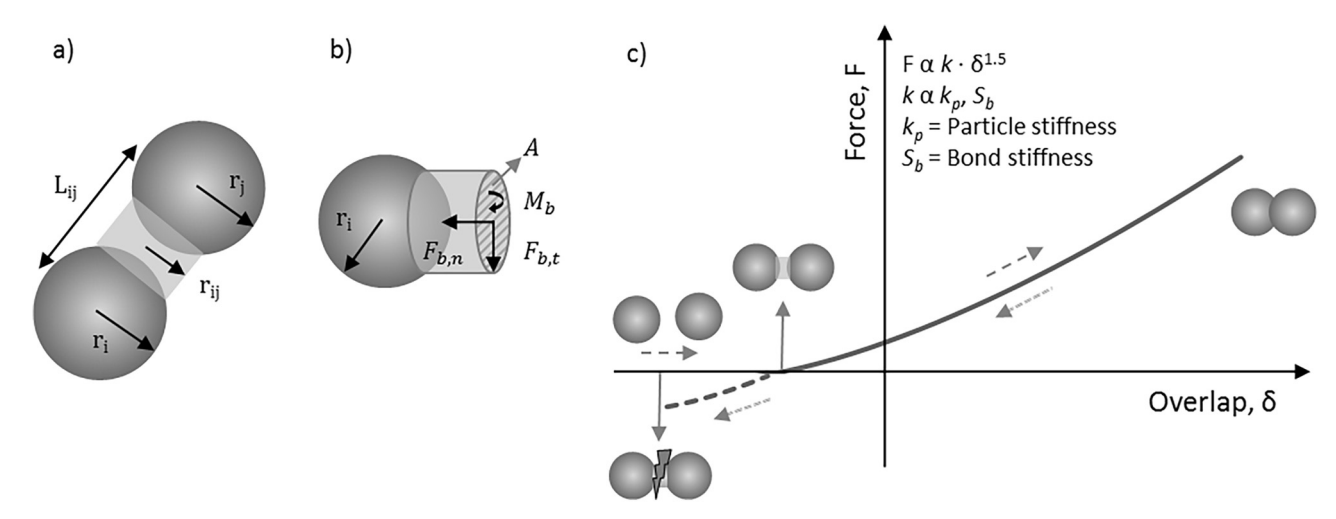


Fig. 2. (a) Solid bond between two particles; (b) Components of a solid bond; (c) Schematic graph of the Hertzian-bond contact model in normal direction.

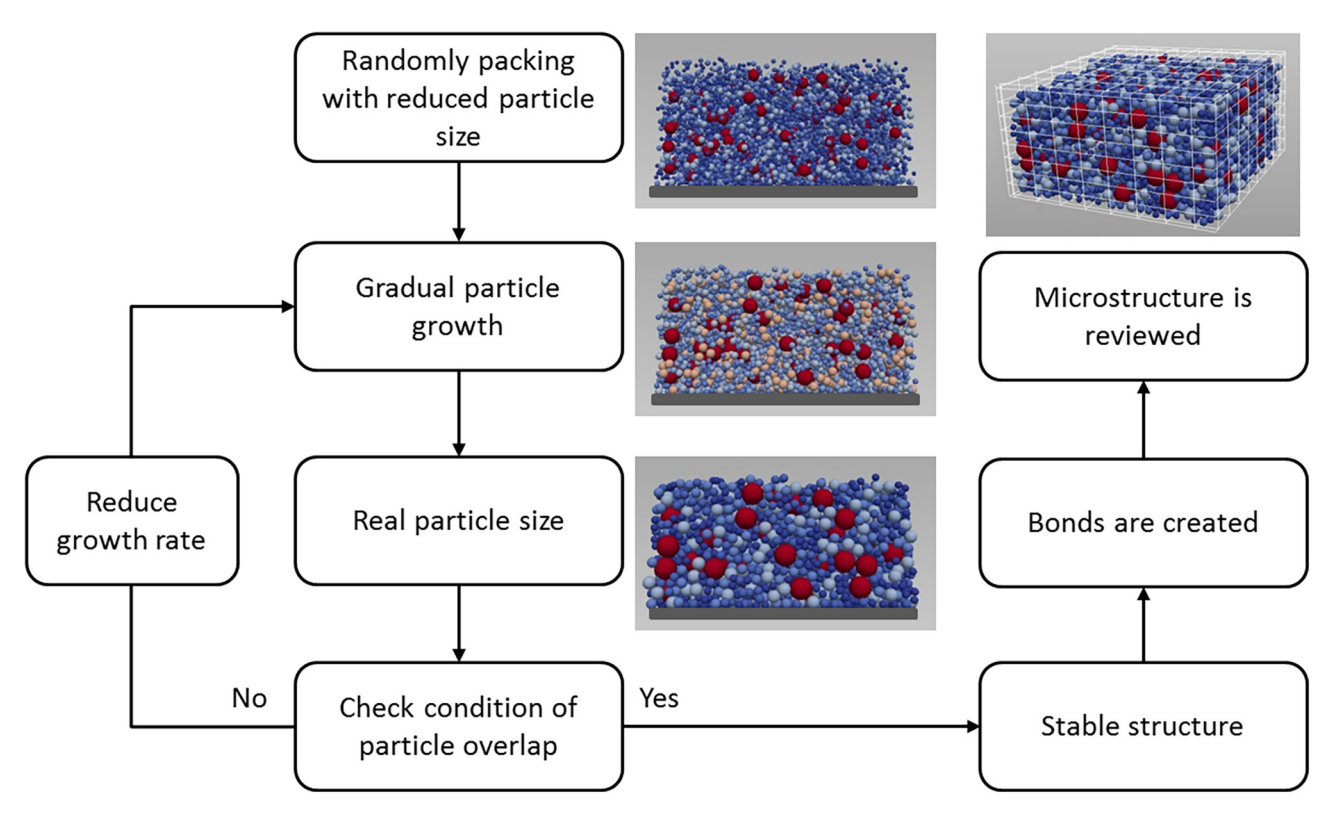


Fig. 3. Flowchart describing the structure generation procedure.

other research groups [9,10,23,24], brings the possibility to create a dense packing without performing any compression of the particles or implementing any gravity-driven packing or additional drag force, which certainly has an effect on the final microstructure. Once the active material particles were correctly set, bonds between them were computed in order to represent the binder phase. It must be noted that no effect of gravity was regarded throughout the simulation due to the fact that particles lay in the micrometer size range.

Finally, the generated structure was reviewed to examine if the porosity as well as the electrode thickness were correctly reproduced. The latter was estimated by summing every particle z-position with its corresponding radius and taking the maximum

value. In the case of determining the electrode porosity, the procedure was considerably more laborious and consisted in calculating local porosity values within the structure. Hence, the assembly was at first divided into a series of voxels as it is displayed in Fig. 4. The porosity of each voxel was the total solid volume occupied by the particles which are fully within the voxel plus the contributing volume of particles partially inside the voxel divided by the volume of the voxel. That is, depending on their relative position within the voxel, the volume of the particles to be considered was calculated differently, giving rise to several possible cases (Fig. 4). Particles corresponding to type *a* were entirely within the boundaries of the voxel and, therefore, their volume calculation was performed as

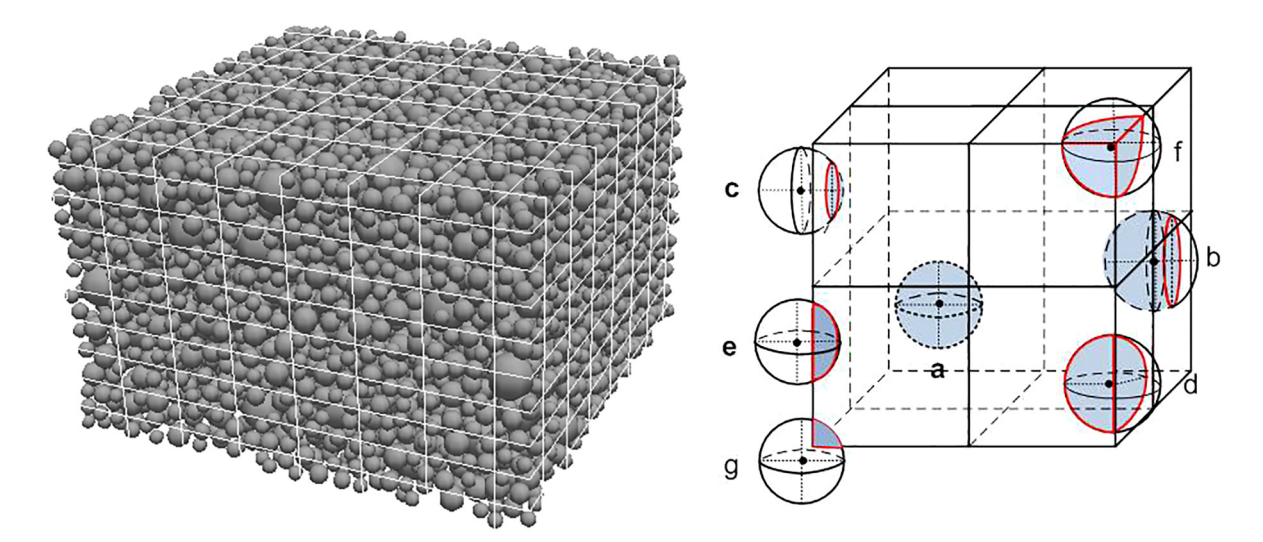


Fig. 4. Left: The electrode structure is divided into 512 voxels along *x*, *y* and *z* direction. Right: 3D schematical illustration of all possible cases for a particle to be placed regarding a certain voxel. Voxels are further divided into smaller units.

$$V_a = \frac{4}{3}\pi r^3 \tag{15}$$

where r is regarded as the particle radius. Likewise, groups b and c gathered the particles whose center points were either inside or outside the voxel but which were cut off by one block plane. The corresponding partial volume was determined by the well-known formula for spherical caps:

$$V_{\textit{spherical cap}} = \frac{\pi h^2}{3} (3r - h) \tag{16}$$

h being the height of the spherical cap. However, if particles cut off by two or three voxel planes were taken into account (groups d,e,f and g), the formulas were no longer adequate. For the explicit purpose of regarding these particles, all voxels were further divided into a series of small voxels, here called units. Thus, every particle being part of one of these critical groups was crossed by numerous units. Each unit was analyzed and by comparing its distance to the particle center point to its distance to the particle radius, it could be appointed whether the unit was inside the particle or not. Finally, the volume of all units inside particles was added, which corresponds to the volume of particles inside the examined voxel. This method to calculate the porosity of a particulate layer proves to be extremely accurate. Unquestionably, its efficiency depends on how small the voxels and the units are. In order to achieve reliable results while guaranteeing reasonable computational time, the simulation box was divided in 8 voxels per width, length and height, respectively. Likewise, each voxel was divided into 512 units.

4. Results and discussion

4.1. Model calibration

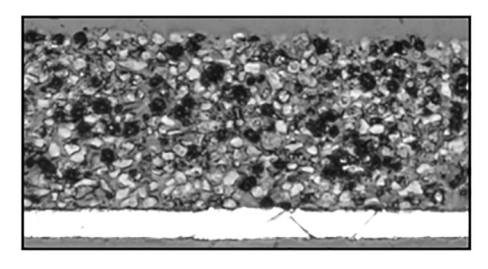
As it has been mentioned, the binder contributes to the overall bulk stiffness. For this reason, the determination of the bond stiffness is key to describe the mechanical behavior of the electrode. In this work, nanoindentation experiments were simulated in order to determine this value. Nanoindentation is a well-known method which has already been confirmed to be a great tool for the purpose of characterizing the mechanical properties of particulate coatings, as shown by Barth et al. [25]. Combination of purely experimental investigation with DEM simulations has been successfully performed by Schilde et al. [26] with the aim of investigating micromechanical properties of aggregates. The idea thereby is to calibrate the bond stiffness by reproducing the macroscopic behavior of the electrode during nanoindentation measurements.

The first step was to reproduce the structure of the electrode (C1) following the guideline described in the previous section. Taking into consideration the laser diffraction results, five particle sizes were reckoned and their quantity was calculated for a representative square electrode section of 150 μ m edge length. A total of 8251 particles were simulated. In this work, 20% of the Raleigh

time step was taken so no disturbance propagated further than a particle's immediate neighbor within one time step. This value corresponded to a time step of 10^{-10} s. As it has already been explained, particles half the real size were generated within the boundaries of the simulation box and progressively enlarged until the real size was achieved. The particle growth rate was fixed at $5.28 \cdot 10^{-6} \, \text{cm s}^{-1}$. Bonds were created and the binder content, 4 wt% as displayed in Table 1, was captured by setting f_b to 0.24 (Eq. (6)). Finally, the generated structure was reviewed regarding its porosity and thickness. The numerically calculated thickness was 76.492 μm, presenting a deviation of 0.008 μm from the experimental value. The porosity, computed with the in-house designed method, was 0.451 and the experimental porosity was 0.45, as shown in Table 1. The remarkable accuracy of the whole process is therefore confirmed. Fig. 5 illustrates the simulation structure of electrode C1 along with a cross-section SEM image of the real manufactured anode C1.

Once the structure was reconstructed, the force acting on a mesh representing the flat punch indenter was calculated analogous to the experimental measurements. The procedure started with the indenter stressing the electrode till a maximum displacement of 7.65 µm, followed by the unloading of the indenter and returning to its initial position. The indentation rate was 0.15 μm s⁻¹ and it was held constant during loading and unloading, in order to reproduce the experimental conditions. Fig. 6 shows the simulation setup (left) as well as three snapshots at different simulation steps (right). In order to better clarify the process, the nanoindenter is not displayed so the displacement of the particles with reference to their initial positions can be easily discerned. It can be seen, that the particles are motionless at the beginning of the simulation (all are in dark blue displayed). As the nanoindenter penetrates into the electrode, the particles start to move from their original location until h_{max} is reached (Fig. 6b). At this point, the maximum displacement of the particles is achieved. Finally, the nanoindenter gets back to its initial position (Fig. 6c). The microstructure of the electrode is only partially recovered as a result of plastic deformation.

A sensitivity analysis was performed in order to assess the influence of the individual input parameters on the mechanical macroscopic response. For convenience, the effect of single variables was evaluated within a certain realistic range while other parameters were fixed. Poisson ratio and coefficient of restitution of active material particles proved to have a minor impact on the forcedisplacement curve, possibly due to the prevailing effect of the bonds on the bulk mechanics. As a result, these parameters were taken from the literature and left constant for all simulations [27–29]. On the contrary, Young's modulus of active material particles and bond stiffness were confirmed to be key values in the determination of the bulk behavior. The values of Young's modulus for MCMB particles vary from 0.03 to 10 GPa according to the literature [28,29]. Hence, single particle nanoindentation experiments were performed in order to narrow this range and assure a reliable base value for the simulation. Using a flat punch indenter, a host of



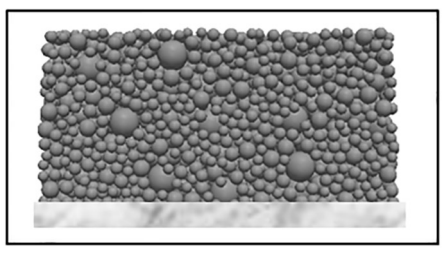
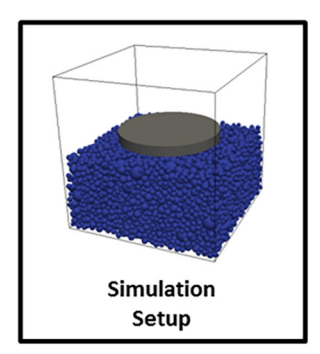


Fig. 5. Cross-section SEM image of the manufactured anode C1 and its analogous numerically generated structure. Bonds between particles are not displayed.



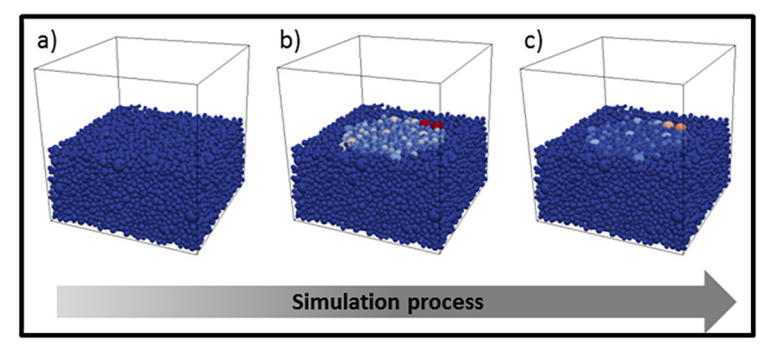


Fig. 6. Schematic of the nanoindentation simulation setup showing the nanoindenter above the electrode structure at the beginning of the process (left). Snapshots of the nanoindentation simulation without showing the nanoindenter for better understanding (right); (a) At the beginning of the simulation; (b) After loading till the maximal displacement is reached; (c) After completely unloading the nanoindenter. The colors are accounted for the displacement of the particles with reference to their initial positions, ranging from red. (For interpretation of the references to color in this figure legend, the reader is referred to the web version of this article.)

particles were indented to a maximum depth of 10% of their diameter. The Young's modulus was obtained from the slope of the unloading curves at maximum load, as shown by Heinrich et al. [30]. The average Young's modulus was 0.32 ± 0.18 GPa, which was assumed as the initial value for the simulation. No literature data were found concerning the binder stiffness of the SBR/CMC mixture. $1 \cdot 10^{10}$ N m $^{-3}$ was chosen as the initial value for the further iterative calibration. The calibration of the model was performed by iteratively coupling the two aforementioned parameters in order to accurately reproduce the experimental force-displacement curve. This procedure was completed for a Young's modulus of 0.45 GPa and an area-related bond stiffness of 13.5 \cdot 10 10 N m $^{-3}$. Table 2 lists the parameters and their corresponding definitive and calibrated values used in the simulation.

Another aspect that needed to be regarded was the original position of the particles within the boundaries. It became evident that depending on where the particles were positioned, the results could deviate considerably. Therefore, all simulations were run five times with different stochastic initial packings. The presented result comprises the mean force-displacement curve and the corresponding standard deviation. Likewise, the mean experimental force-displacement curve of the 80 measurements is displayed along with the standard deviation.

Fig. 7 shows the experimental and simulative outcome. It can be stated that both mean curves are in good agreement; hence the simulation was able to properly capture the macroscopic elastoplastic behavior of the anode. Micromechanical properties of such particulate structures often exhibit a lognormal distribution due to differences in contact area between particles and interaction forces [25]. This fact directly leads to a distribution of the bulk mechanical properties and, consequently, a different force-displacement curve after every nanoindentation. As it can be seen in Fig. 7, such a deviation can be accomplished via simulations as well. The maximum indentation force obtained via simulation differs only 0.45% from the experimental value, as it is shown in Table 3. Even though the simulated loading curve was extremely close to the experimental one, the plastic behavior could not be fully captured

Table 2Calibrated DEM simulation parameters.

Parameter	Value	
Density, $ ho$	$2.2~{\rm g~cm^{-3}}$	
Young's modulus, E	0.45 GPa	
Poisson ratio, v	0.30	
Coefficient of restitution, e	0.25	
Area-related bond stiffness, S_b	$13.5 \cdot 10^{10} \text{ N m}^{-3}$	
Damping factor, α	0.95	

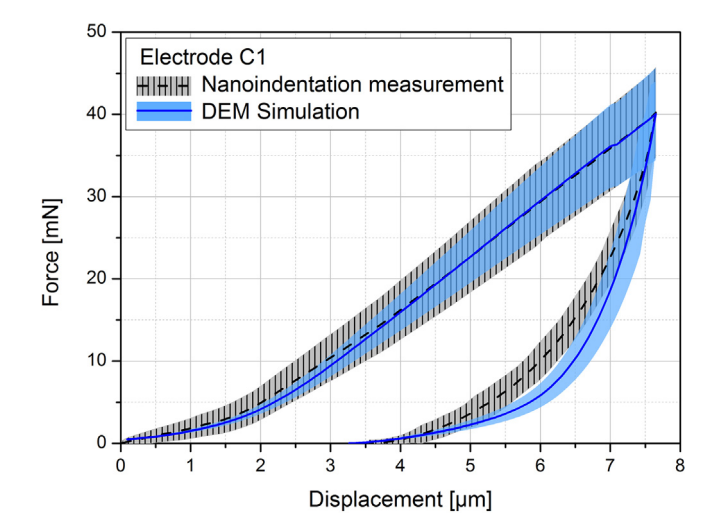


Fig. 7. Comparison of measured and simulated force-displacement curves for electrode C1.

during unloading. Simulations were run with a damping coefficient of 0.95, leading to a reduction of restoring forces and torques as it has been explained in the Methodology Section. This parameter was determined with the final set of Young's modulus and bond stiffness. Simulations were carried out under different damping coefficient values ranging from 0.7 to 1.0 (force was not dissipated). However, in light of the results, it is believed, that a more sophisticated damping formulation may be required in future work to fully capture the macroscopic plastic behavior of the anode.

4.2. Model validation

The aim of the experimental validation was to determine whether the structure generation method, including the chosen contact model, was able to reliably predict the mechanical behavior of different anode structures. For this purpose, two anodes, V1 and V2, were manufactured with different structural properties (Table 1). As it has already been shown, anode V1 was composed of coarser particles maintaining the original amount of binder of anode C1, while anode V2 was thicker and had a higher binder content in comparison to anode C1. The porosity of V1 and V2 was greater as that of C1, reaching a value of 0.59. Due to these variations, all three electrodes presented different structural characteristics.

Table 3 Experimental and simulation quotients of elastic and total deformation energies (W_{el}/W_{tot}) and plastic and total deformation energies (W_{pl}/W_{tot}) as well as maximal indentation force (F_{max}) for the electrode structures.

Electrode	Parameter	Experimental nanoindentation	Simulation	Deviation [%]
C1	W _{el} /W _{tot} [-]	0.33 ± 0.07	0.27 ± 0.03	18.18%
	W_{pl}/W_{tot} [-]	0.67 ± 0.07	0.73 ± 0.03	8.96%
	F _{max} [mN]	40.05 ± 6.47	40.23 ± 4.00	0.45%
V1	W_{el}/W_{tot} [-]	0.30 ± 0.02	0.32 ± 0.01	6.53%
	W_{pl}/W_{tot} [-]	0.70 ± 0.02	0.68 ± 0.01	2.83%
	F _{max} [mN]	62.71 ± 11.56	62.69 ± 7.52	0.0003%
V2	W_{el}/W_{tot} [-]	0.31 ± 0.03	0.29 ± 0.0002	6.45%
	W_{pl}/W_{tot} [-]	0.69 ± 0.03	0.71 ± 0.0002	2.90%
	F _{max} [mN]	27.11 ± 6.25	25.95 ± 3.11	4.28%

The validation of the numerical model required a comparison between the numerically predicted mechanical behavior and that actually obtained via nanoindentation experiments. Considering anode V1, five particle size fractions were simulated based on the laser diffraction measurements within a representative square electrode section of 200 µm edge length. At the beginning, 565 particles half the real size were generated and progressively enlarged until the real size was achieved. The particle growth rate was fixed at $6.14 \cdot 10^{-6}$ cm s⁻¹, guaranteeing a stable system. Bonds were created and the binder content was captured by setting f_b to 0.25 (Eq. (6)). Finally, the numerically calculated thickness was 79.82 μm (experimental thickness corresponded to 79.86 μm) and the porosity was 0.593 (experimental porosity equaled 0.59). The procedure to numerically generate anode V2 was the same as for anode C1. A total of 7693 particles were simulated under the same conditions of growth rate. The value of f_b was 0.42, for the purpose of capturing the higher binder content by creating a greater number of bonds between particles. Both porosity and thickness were calculated for these structures. The numerically calculated thickness was $96.15 \,\mu m$ and the porosity was 0.587, extremely close to the correspondent experimental values: 96.11 um and 0.59. respectively. The accuracy of the whole process could be confirmed again since the values only differ slightly from the experimental data. Schematic views of the simulation structures of electrodes V1 and V2 are illustrated in Fig. 8 along with corresponding cross-section SEM images of the real manufactured anodes.

The indentation rate was once again $0.15~\mu m~s^{-1}$ and it was held constant during loading and unloading, in order to reproduce the experimental conditions. When comparing simulated to

experimental force-displacement curves, it became evident that the model had notable shortcomings for anode V1. It was therefore required to increase the precision of the simulations. In light of the fact that the binder composition was the same for structures C1 and V1, it was decided not to modify the bond stiffness. Consequently, the Young's modulus of the particles had to be adjusted. In fact, a dependence of elasticity and particle size has already been mentioned by Barth et al. [25]. It was confirmed that the fitting of the experimental and simulation curves worked better for greater values of Young's modulus. The calibration procedure concluded with a Young's modulus of 0.52 GPa.

Fig. 9 displays the conclusive force-displacement curves obtained via simulation and their analogous experimental curves for electrode V1 (left) and V2 (right). Table 3 gathers the information related to elastic and plastic deformation energy quotients of these structures along with electrode C1. The accuracy of the method predicting the mechanical behavior of different anode structures can be underlined by taking a look at the minor deviations between numerical and experimental values.

The goal of this work was not meant to pursue a comparison among the manufactured electrodes, but rather to demonstrate that the developed DEM-based procedure was able to structurally and mechanically represent different electrode coatings. Bearing this in mind, Fig. 10 presents an overview comparing analytical and numerical results for the three manufactured and simulated electrodes. On the one hand, the model could accurately represent the maximum indentation force for smaller (anode C1) and coarser particle-based structures (anode V1). Closely examining these two structures and without overlooking their differences in porosity, it

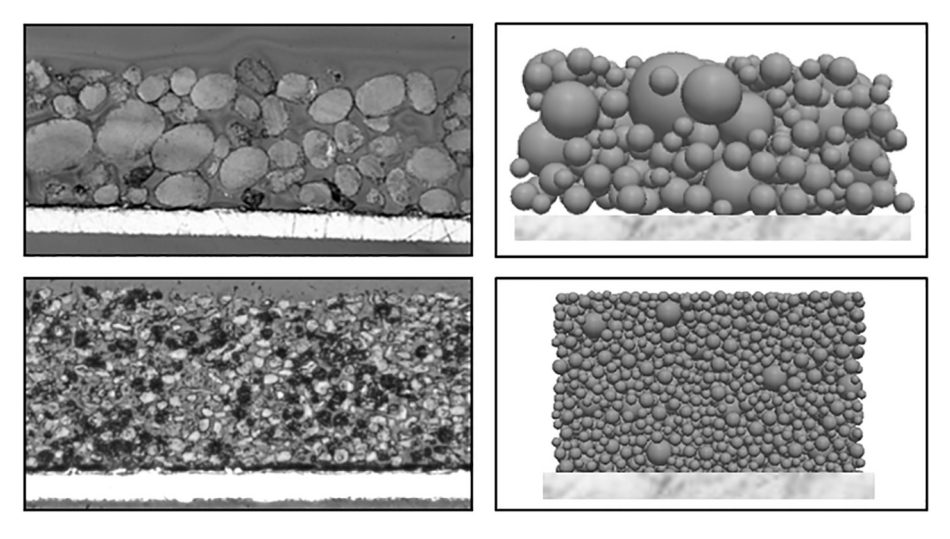


Fig. 8. Left: Cross-section SEM image of the manufactured electrodes V1 (top) and V2 (bottom). Right: Analogous three-dimensional numerically generated structures (right). Bonds between particles are not displayed.

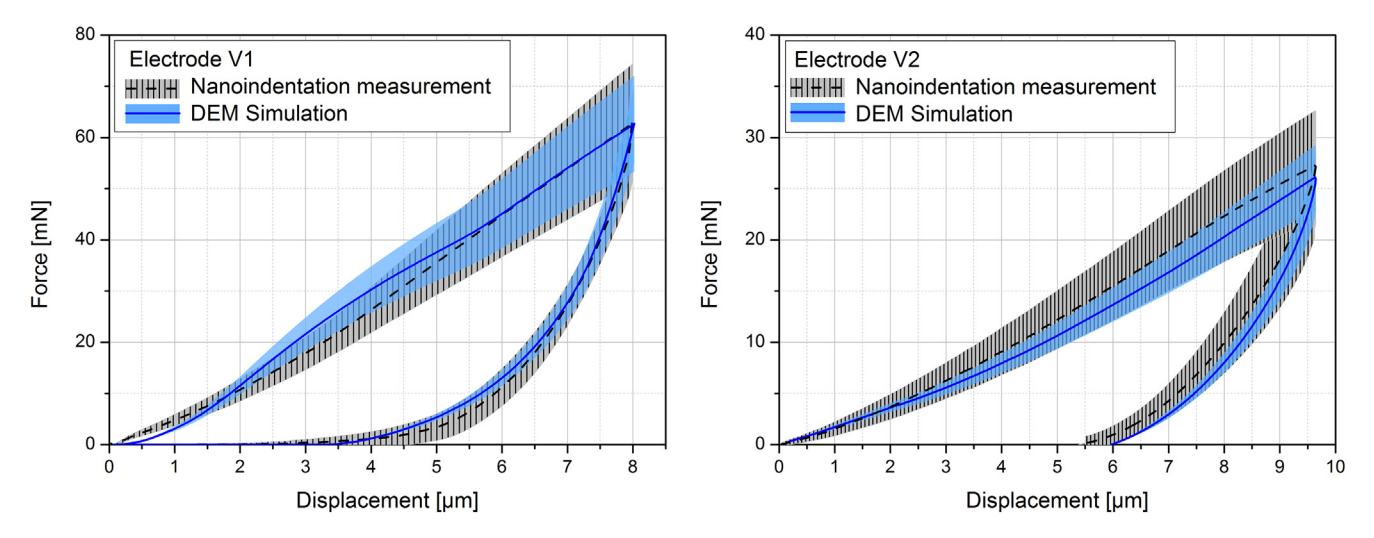


Fig. 9. Comparison of measured and simulated force-displacement curves for electrodes V1 (left) and V2 (right).

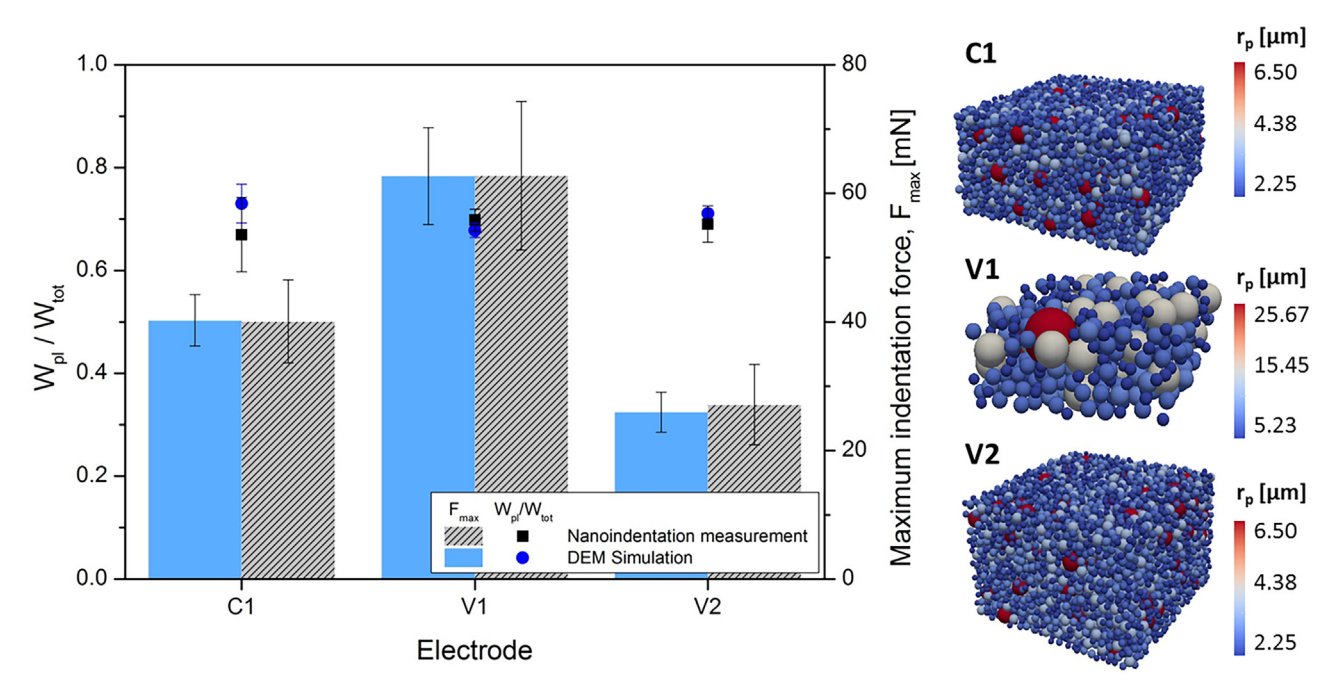


Fig. 10. Overview of analytical and numerical results for manufactured and simulated electrodes. Right: Three-dimensional numerically generated structures V1, C1 & C2. The colors are accounted for the particle radius. Bonds between particles are not displayed. (For interpretation of the references to color in this figure legend, the reader is referred to the web version of this article.)

can be discerned that a decrease in particle size leads to a reduced maximum indentation force. This fact has already been experimentally observed for other particulate coatings, i.e., for alumina nanoparticulate coatings, and it is related to the number of particle contacts [31]. Coarser particles have fewer contacts, resulting to a straightforward transmission of the force to the substrate, here the current collector. Evaluating the presented results, the simulations were able to capture this phenomenon. On the other hand, this value could also be reached when varying the binder content (anode V2). The maximum force obtained by indenting anode V2 is lower than that of anode C1 due to the amount of binder and the increment in porosity, which reduces the number of particle contacts and therefore decreases particle constraint within the structure. By means of increasing f_b to 0.42 and adjusting the porosity likewise, the simulation of anode V2 was able to reproduce this behavior as well. Thus, not only the properties of the

active material particles were well reproduced, but also the properties related to the binder. On account of this, the calibrated bond stiffness proved to be correct to represent the elasto-plastic behavior of the SBR/CMC binder.

5. Conclusions

Taking into consideration the discrete nature of composite lithium-ion battery electrodes, this study proposed a simulation procedure and a proper DEM contact model to reproduce the microstructural and mechanical properties of such structures. The novelty of this work lies in the fact that real experimental values of porosity as well as particle size distribution and electrode thickness could be replicated via simulations. Moreover, the macromechanical properties could also be captured by means of combining nanoindentation measurements with simulations.

Three electrodes were numerically generated by firstly inserting the size-reduced active material particles within the simulation domain. The radii of the particles were gradually increased to match the real particle size distribution, assuring a stable system while keeping a reasonable CPU time. Subsequently, bonds between active material particles were implemented in order to represent the binder phase, which plays a fundamental role in the macromechanical properties of the electrode. For this reason, a bond-contact model based on the Hertz contact model was adapted to appropriately describe the elasto-plastic behavior of the interconnected network of binder and active material particles. Ultimately, the final electrodes were examined regarding their porosity and thickness. These results revealed the good agreement between simulations and real manufactured electrodes. Furthermore, the anodes were mechanically analyzed via flat-punch nanoindentation. By reproducing the experiment, the bond stiffness was calibrated for the so called anode C1. Due to the fact that the binder composition was not altered, the Hertzian-bond contact model could be validated for the remaining two anodes (V1 & V2) without any required modification of bond stiffness. On account of the presented force-displacement curves, it could be concluded that the DEM procedure to generate targeted microstructures, in combination with the enhanced Hertzian-bond contact model, offers an interesting tool for analyzing such electrode structures.

Providing more realistic numerical microstructures that better reflect the macromechanics of lithium-ion battery electrodes constitutes a valuable physical basis for a great number of applications. Future research may adopt the given method to quantitatively assess the effect of structural and mechanical parameters. Exemplarily, the applications of this work may comprise analyzing elastic and fracture properties of porous electrodes under different stress conditions and/or examining possible particle rearrangements with regard to diverse electrode compositions. Additionally, by including carbon black particles, this method may be useful to investigate the percolation threshold and predict electrode structures giving certain morphological parameters.

Acknowledgements

The authors gratefully acknowledge the financial support by the Federal Ministry for Economic Affairs and Energy (BMWi) within the research project "DaLion - Datamining in der Produktion von Lithium-Ionen Batteriezellen". Furthermore, we would like to express our sincere thanks to Rahul Mohanty, Boyue Zhou, Lennart Kleinfeldt and Axel Rosenkranz for their valuable assistance.

References

- S.W. Peterson, D.R. Wheeler, Direct measurements of effective electronic transport in porous Li-Ion Electrodes, J. Electrochem. Soc. 161 (14) (2014) A2175–A2181.
- [2] H. Bockholt, M. Indrikova, A. Netz, F. Golks, A. Kwade, The interaction of consecutive process steps in the manufacturing of lithium-ion battery electrodes with regard to structural and electrochemical properties, J. Power Sources 325 (2016) 140–151.
- [3] A. Michaels, H. Bockholt, W. Haselrieder, A. Kwade, Governing electrode properties using classified battery active materials, in: European Symposium on Comminution and Classification S. 302–305, 2013.

- [4] V.A. Sethuraman, M.J. Chon, M. Shimshak, V. Srinivasan, P.R. Guduru, In situ measurements of stress evolution in silicon thin films during electrochemical lithiation and delithiation, J. Power Sources 122 (2010) 195–5062.
- [5] A. Mukhopadhyay, A. Tokranov, X. Xiao, B.W. Sheldon, Stress development due to surface processes in graphite electrodes for Li-ion batteries: a first report, Electrochim. Acta 66–28 (2012).
- [6] E. Chason, B.W. Sheldon, Monitoring stress in thin films during processing, Surf. Eng. 19–387 (2003).
- [7] A. Mukhopadhyay, B.W. Sheldon, Deformation and stress in electrode materials for Lithium-ion batteries, Prog. Mater Sci. 63 (2014) 58–116.
- [8] P.A. Cundall, O.D.L. Strack, Geotechnique 29 (1979) 47-65.
- [9] L.C.R. Schneider, C.L. Martin, Y. Bultl, D. Bouvard, E. Siebert, Discrete modelling of the electrochemical performance of SOFC electrodes, Electrochim. Acta 52 (1) (2005) 314–324.
- [10] Liu, C.L. Martin, G. Delette, J. Laurencin, D. Bouvard, T. Delahaye, Microstructure of porous composite electrodes generated by the discrete element method, J. Power Sources 196 (4) (2011) 2046–2054.
- [11] M. Forouzan, C. Chao, D. Bustamante, B. Mazzeo, D. Wheeler, Experiment and simulation of the fabrication process of lithium-ion battery cathodes for determining microstructure and mechanical properties, J. Power Sources 312 (2016) 172–183.
- [12] L. Froböse, P. Titscher, B. Westphal, W. Haselrieder, A. Kwade, Mercury intrusion for ion- and conversion-based battery electrodes – structure and diffusion coefficient determination, Mater. Charact. 133 (2017) 102–111, https://doi.org/10.1016/j.matchar.2017.09.002.
- [13] A.C. Fischer-Cripps, A review of analysis methods for sub-micron indentation testing, Vacuum 58 (2000) 569–585.
- [14] H. Hertz, Die Prinzipien der Mechanik, in neuem Zusammenhange dargestellt, J. Reine Angew. Math. 92 (1881) 156–171.
- [15] D.O. Potyondy, P.A. Cundall, A bonded-particle model for rock, Int. J. Rock Mech. Min. Sci 41 (2004) 1329–1364.
- [16] D. Zabulionis, R. Kacianauskas, D. MArkauskas, J. Rojek, An investigation of nonlinear tangential contact behaviour of a spherical particle under varying loading, Tech. Sci. 60, No. 2, 2012.
- [17] R.D. Mindlin, Compliance of elastic bodies in contact, J. Appl. Mech. 16 (1949) 259–268.
- [18] S. Beinert, C. Schilde, A. Kwade, Simulation of stress energy and grinding media movement within a wet operated annular gap mill using the discrete element method, Chem. Eng. Technol. 35 (2012) 1899–2059.
- [19] S. Lim, S. Kim, K. Ahn, The effect of binders on the rheological properties and the microstructure formation of lithium-ion battery anode slurries, J. Power Sources 299 (2015) 221–230.
- [20] S. Luding, Introduction to discrete element methods: basics of contact force models and how to perform the micro-macro transition to continuum theory, Discrete Modell. Geomater. 785–826 (2008).
- [21] Subhash Thakur, Micromechanical analysis of cohesive granular materials using the discrete element method with an adhesive elasto-plastic contact model, Granular Matter 16 (3) (2014) 383–400.
- [22] C. Kloss PS, A. Aigner, S. Amberger, C. Goniva. LIGGGHTS User Manual., 2013.
- [23] G. Pianet, F. Bertrand, D. Vidal, B. Mallet, Discrete element method-based models for the consolidation of particle packings in paper-coating applications, I. Chem. Eng. 6 (2011) 44–54.
- [24] X. Liu, C. Martin, D. Bouvard, S. Iorio, J. Laurencin, G. Delette, Strength of highly porous ceramic electrodes, J. Am. Ceram. Soc. 94 (2011) 3500–3508.
- [25] N. Barth, C. Schilde, A. Kwade, Influence of particle size distribution on micromechanical properties of thin nanoparticulate coatings, Phys. Proc. 40 (2013) 9–18.
- [26] C. Schilde, C. Burmeister, A. Kwade, Measurement and simulation of micromechanical properties of nanostructured aggregates via nanoindentaion and DEM-simulation, Powder Technol. 259 (2014) 1–13.
- [27] K. Takahashi, K. Higa, S. Mair, M. Chintapalli, N. Balsara, V. Srinivasan, Mechanical degradation of graphite/PVDF composite electrodes: a modelexperimental study, J. Electrochem. Soc. 163 (3) (2016) 385–395.
- [28] B.T. Kelly, Physics of Graphite, Applied Science, London, 1981.
- [29] H. Marsh, E.A. Heintz, F. Rodríguez-Reinoso, Introduction to Carbon Technologies, University of Alicante, 1997.
- [30] C. Heinrich, A.M. Waas, A.S. Wineman, Determination of material properties using nanoindentation and multiple indenter tips, Int. J. Solids Struct. 46 (2009) 364–376.
- [31] C. Schilde, B. Westphal, A. Kwade, Effect of primary particle morphology on the micromechanical properties of nanostructured alumina agglomerates, J. Nanopart. Res. 14 (3) (2012).